Improved one-dimensional model potentials for strong-field simulations

Szilárd Majorosi,[1] Mihály G. Benedict,[1] and Attila Czirják[1,2,*]
[1]*Department of Theoretical Physics, University of Szeged, Tisza L. krt. 84-86, H-6720 Szeged, Hungary*
[2]*ELI-ALPS, ELI-HU Non-Profit Ltd., Dugonics tér 13, H-6720 Szeged, Hungary*

(Received 11 June 2018; published 1 August 2018)

Based on a plausible requirement for the ground-state density, we introduce an alternative one-dimensional (1D) atomic model potential for the 1D simulation of the quantum dynamics of a single active electron atom driven by a strong, linearly polarized few-cycle laser pulse. The form of this density-based 1D model potential also suggests improved parameters for other well-known 1D model potentials. We test these 1D model potentials in numerical simulations of typical strong-field physics scenarios and we find an impressively increased accuracy of the low-frequency features of the most important physical quantities. The structure and the phase of the high-order harmonic spectra also have a very good match to those resulting from the three-dimensional simulations, which enables one to fit the corresponding power spectra with the help of a simple scaling function.

DOI: 10.1103/PhysRevA.98.023401

I. INTRODUCTION

Atomic and molecular physics has witnessed a revolution due to the appearance of attosecond pulses [1–14]. True understanding of the phenomena in attosecond and strong-field physics often needs the quantum evolution of an involved atomic system driven by a strong laser pulse [15–21]. However, an analytic or even numerically exact solution of the corresponding Schrödinger equation is beyond reach in this nonperturbative range, except for the simplest cases. Therefore, approximations are unavoidable and very important.

For linearly polarized pulses, the main dynamics happens along the electric field of the laser pulse which underlies the success of some one-dimensional (1D) approximations [22–33]. These typically use various 1D model potentials to account for the behavior of the atomic system. However, the particular model potential chosen heavily influences the 1D results, and their comparison with the true three-dimensional (3D) results is usually nontrivial. One of these important deviations is that the dipole moment, created by the same electric field, may have much larger or much smaller values in the 1D than in the 3D simulation.

In the present paper, we introduce and test 1D atomic model potentials for strong-field dynamics driven by a linearly polarized laser pulse. Our key idea is to require the ground-state density of the 1D model to be equal to the reduced 3D ground-state density, obtained by integrating over spatial coordinates perpendicular to the direction of the laser polarization. According to density functional theory, this 1D ground-state density determines the corresponding 1D model potential up to a constant, which we set by matching the ground-state energies. Comparison of the resulting formula with well-known 1D model potentials inspires us to use some of the latter with improved parameters. Then we test these improved 1D model potentials by applying them in careful numerical simulations of strong-field ionization by a few-cycle laser pulse. Based on these results we make a conclusion about the best of these 1D model potentials. We use atomic units in this paper.

II. 3D AND 1D MODEL SYSTEMS

A. 3D reference system

First, we define the 3D system which we aim to model in one dimension. We write the Hamiltonian H_0^{3D} of a 3D hydrogen atom or hydrogenlike ion in cylindrical coordinates $\rho = \sqrt{x^2 + y^2}$ and z as

$$H_0^{3D} = T_z + T_\rho - \frac{Z}{\sqrt{\rho^2 + z^2}}, \tag{1}$$

where Z is the charge of the ion core ($Z = 1$ for hydrogen) and the two relevant terms of the kinetic energy operator are given by

$$T_\rho = -\frac{1}{2\mu}\left[\frac{\partial^2}{\partial\rho^2} + \frac{1}{\rho}\frac{\partial}{\partial\rho}\right], \qquad T_z = -\frac{1}{2\mu}\frac{\partial^2}{\partial z^2}, \tag{2}$$

where μ denotes the (reduced) mass of the reduced system. By solving the equation

$$H_0^{3D}\psi_{100}(z,\rho) = E_0\psi_{100}(z,\rho), \tag{3}$$

we get the well-known ground-state energy and wave function of the Coulomb problem [34,35] as

$$E_0 = -\frac{\mu Z^2}{2}, \qquad \psi_{100}(z,\rho) = \mathcal{N}\, e^{-\mu Z\sqrt{\rho^2+z^2}}, \tag{4}$$

where $\mathcal{N}$ is a real normalization factor. We consider the action of a linearly polarized laser pulse on this atomic system in the dipole approximation by the potential

$$V_{\text{ext}}(z,t) = z\mathcal{E}_z(t) \tag{5}$$

*czirjak@physx.u-szeged.hu

and seek solutions of the time-dependent Schrödinger equation

$$i\frac{\partial}{\partial t}\Psi^{3D}(z,\rho,t) = \left[H_0^{3D} + V_{ext}(z,t)\right]\Psi^{3D}(z,\rho,t) \quad (6)$$

that start from the $\psi_{100}(z,\rho)$ ground state at $t=0$, and we compute it up to a specified time T_{max}. This time-dependent Hamiltonian still has axial symmetry around the direction of the electric field of the laser pulse, which makes the use of cylindrical coordinates practical. For the efficient numerical solution of the time evolution in real space, we use the algorithm described in [36] which incorporates the singularity of the Hamiltonian directly, using the required discretized Neumann and Robin boundary conditions.

B. 1D model system

In order to model the above-described 3D time-dependent process in one dimension, it is customary to assume a 1D atomic Hamiltonian of the following form:

$$H_0^{1D} = T_z + V_0^{1D}(z), \quad (7)$$

where $V_0^{1D}(z)$ is an atomic model potential of choice. Then we seek solutions of the time-dependent Schrödinger equation

$$i\frac{\partial}{\partial t}\Psi^{1D}(z,t) = \left[H_0^{1D} + V_{ext}(z,t)\right]\Psi^{1D}(z,t), \quad (8)$$

where the external potential $V_{ext}(z,t)$ is given in Eq. (5). In this article we introduce an alternative form of $V_0^{1D}(z)$ to model strong-field processes physically as correctly as possible. But before doing so, let us shortly recall some of the 1D potentials used earlier. We then propose certain improvements of these known formulas aiming that the resulting 1D simulations reproduce the 3D system's strong-field response quantitatively correctly.

C. Conventional 1D model potentials

There are a number of well-known 1D atomic model potentials in the literature [26–28], having their advantages and disadvantages. Here we summarize the basics of two of these, which we think to be the most important for the modeling of strong-field phenomena.

The soft-core Coulomb potential is defined as

$$V_{0,Sc}^{1D}(z) = -\frac{Z}{\sqrt{z^2+\alpha^2}}, \quad (9)$$

where the smoothing parameter α is usually adjusted to match the ground-state energy to a selected single electron energy. For $\mu=1$, $Z=1$, and $\alpha^2=2$, its ground-state energy and ground state can be used as a 1D model hydrogen atom:

$$E_{0,Sc} = -\frac{1}{2}, \quad \psi_{0,Sc}(z) = \mathcal{N}_{Sc}(1+\sqrt{z^2+2})e^{-\sqrt{z^2+2}}, \quad (10)$$

where $\mathcal{N}_{Sc}$ is the normalization factor. The most important features of this model potential are that it is a smooth function, and it has an asymptotic Coulomb form and Rydberg continuum. The energy of its first excited state is $E_{1,Sc} = -0.2329034$.

The 1D Dirac delta potential [29–31]

$$V_{0,DD}^{1D}(z) = -Z\delta(z) \quad (11)$$

has the following ground-state energy and ground state:

$$E_{0,DD} = -\frac{Z^2}{2}, \quad \psi_{0,DD}(z) = \sqrt{Z}e^{-Z|z|}, \quad (12)$$

for $\mu=1$. The singularity of $V_{0,DD}^{1D}(z)$ at $z=0$ is sometimes considered a disadvantage, but this gives rise to a Robin boundary condition, just like the Coulomb singularity does in three dimensions. Note that the ground state eigenfunction of this potential shows the same exponential form and cusp as that of the 3D hydrogen atom, while the corresponding energy eigenvalue is also the same (with $Z=1$).

Despite these facts, the experience shows that Eqs. (9) and (11) do not give strong-field simulation results that would be quantitatively comparable to those of the reference 3D system (cf. [28,37,38]), therefore, the model system parameters need to be manually adjusted, for example, by changing the strength of $V_{ext}(z,t)$.

III. DENSITY-BASED MODEL POTENTIALS

A. Derivation of the 1D analytic model potential

As an alternative to the conventional potentials we now propose another 1D potential to be denoted here by $V_{0,M}^{1D}(z)$. In view of its peculiarities, we then also suggest certain improvements in the previously known 1D model potentials.

Our inspiration of deriving this alternative model potential originated from the ground-state density functional theory of multielectron atoms. More specifically, the following derivation is analogous to the derivation of the Kohn-Sham potential of a helium atom with a single orbital: knowing the correct reduced (single-particle) density [39], one can invert the Schrödinger equation to determine the Kohn-Sham potential [40]. In this way one can model the ground state of the system as accurately as it is possible with a single orbital. However, in the present paper we consider just single active electron atoms and we make the analogous reduction from the 3D electron coordinates to the z coordinate of the single electron.

For developing our 1D model potential, we need the 1D reduced density of the 3D ground state that is defined by

$$\varrho_z^{100}(z) = 2\pi\int_0^\infty |\psi_{100}(z,\rho)|^2\rho\, d\rho. \quad (13)$$

After the substitution of Eq. (4) for the integrand, we can perform this integral analytically, which yields the closed form

$$\varrho_z^{100}(z) = \frac{\mu Z}{2}(2Z\mu|z|+1)e^{-2Z\mu|z|}. \quad (14)$$

Our key idea is now to require the 1D model system to have its ground-state density identical with $\varrho_z^{100}(z)$. According to density functional theory, this 1D ground-state density determines the corresponding 1D model potential $V_{0,M}^{1D}(z)$ up to a constant. We can calculate this potential straightforwardly: we define the ground state of the 1D model atom obviously as $\psi_0(z) = \sqrt{\varrho_z^{100}(z)}$, i.e.,

$$\psi_0(z) = \sqrt{\frac{\mu Z}{2}}\sqrt{2\mu Z|z|+1}e^{-\mu Z|z|}, \quad (15)$$

and then we invert the eigenvalue equation of H_0^{1D} as

$$V_{0,M}^{1D}(z) = E_{0,M} + \frac{1}{\psi_0(z)}\frac{1}{2\mu}\frac{\partial^2}{\partial z^2}\psi_0(z). \quad (16)$$

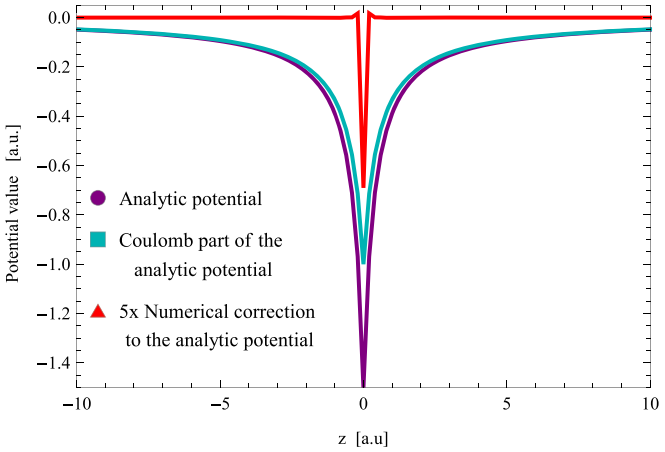

FIG. 1. Plot of the analytic potential (21) (in purple) and its regularized Coulomb part [second term of Eq. (21), in cyan], for $Z = 1$, $\mu = 1$. We also plot the difference $\widetilde{V}^{1D}_{0,M}(z) - V^{1D}_{0,M}(z)$ (see the discussion in Sec. IV) calculated with step size $\Delta z = 0.2$, and magnified by a factor of 5 (in red). This is to illustrate the numerical correction to be introduced by Eq. (26).

After performing the differentiation we get

$$V^{1D}_{0,M}(z) = E_{0,M} + \frac{2\mu^3 Z^4 |z|^2 - \mu Z^2}{(2\mu Z|z| + 1)^2}. \tag{17}$$

In order to determine the ground-state energy, we rewrite this potential as

$$V^{1D}_{0,M}(z) = E_{0,M} + \frac{\mu Z^2}{2} \frac{(2\mu Z|z| + 1)(2\mu Z|z| - 1) - 1}{(2\mu Z|z| + 1)^2}, \tag{18}$$

and then we impose the asymptotic value

$$\lim_{|z|\to\infty} V^{1D}_{0,M}(z) = 0, \tag{19}$$

which yields the ground-state energy

$$E_{0,M} = E_0 = -\frac{\mu Z^2}{2}. \tag{20}$$

Using this value, after some algebraic manipulations we arrive at the following instructive form of our density-based 1D atomic model potential:

$$V^{1D}_{0,M}(z) = -\frac{1}{2\mu} \frac{1}{2^2\left(|z| + \frac{1}{2\mu Z}\right)^2} - \frac{\frac{1}{2}Z}{|z| + \frac{1}{2\mu Z}}. \tag{21}$$

Let us make a few important notes. It is the asymptotic tail of the reduced 1D ground-state density $\varrho^{100}_z(z)$ that determines the ground-state energy $E_{0,M}$ in such a nontrivial way that it is identical to the ground-state energy of the 3D system, E_0. The asymptotic tail of $\varrho^{100}_z(z)$ also determines the regularized 1D Coulomb potential with effective charge $\frac{1}{2}Z$ which is the second term in Eq. (21). This term is dominant over the short-range first term of Eq. (21) not only in the asymptotic tail but also around the center at least by a factor of 2 (see the corresponding curves of Fig. 1). The minima of both terms of $V^{1D}_{0,M}(z)$ at $z = 0$ decrease with increasing Z or μ. For $Z = 1$ and $\mu = 1$, the energy of its first excited state is $E_{1,M} = -0.0904408$ approximately.

B. Improved 1D model potentials

The results of Sec. III A, especially the somewhat surprising value of an effective charge of $\frac{1}{2}Z$, suggested by the second term of the density-based model potential (21), inspire us to use the 1D soft-core Coulomb potential and a 1D regularized Coulomb potential with accordingly modified values of their parameters. As we will see, these modifications lead indeed to improved results in strong-field simulations.

We use $\frac{1}{2}Z$ in the nominator of the soft-core Coulomb potential, which then requires to change also the parameter α in order to maintain that its ground-state energy matches the 3D ground-state energy. These lead us to the following formula of the improved 1D soft-core Coulomb potential with $\mu = 1$:

$$V^{1D}_{0,M,Sc}(z) = -\frac{\frac{1}{2}Z}{\sqrt{z^2 + \frac{1}{4Z^2}}} \text{ with } E_{0,M,Sc} = -\frac{Z^2}{2}, \tag{22}$$

which has the correct $\frac{1}{2}Z/|z|$ asymptotic behavior when $|z| \to \infty$. The energy of its first excited state is $E_{1,M,Sc} = -0.1058670$.

We also introduce the improved 1D regularized Coulomb potential as

$$V^{1D}_{0,M,C}(z) = -\frac{\frac{1}{2}Z}{|z| + a}, \tag{23}$$

where the value of the parameter a is determined by requiring that the ground-state energy is $E_{0,M,C} = -\frac{\mu Z^2}{2}$. For $Z = 1$ we set $a \approx 0.32889$, which yields $E_{0,M,C} \approx -0.5000007$ (for $\mu = 1$). We note that this has been computed numerically with the spatial step size $\Delta z = 0.2$.

The sophisticated numerical method to be outlined in the next section enables us to make additional refinements regarding the 1D density-based potential, as well as the 1D delta potential. These improvements are explained below, especially by the formulas given in Eqs. (26) and (27).

IV. NUMERICAL METHODS OF THE SOLUTION

Usually, the time-dependent Schrödinger equation (8) must be solved numerically in the nonperturbative regime. We discretize the time variable with time steps Δt as $t_k = k\Delta t$, and the spatial coordinate with steps Δz as $z_j = j\Delta z$ (k, j are integer indices). The discretized wave function is written as $\Psi^{1D}(z_j, t_k)$. We write the discretized form of the 1D atomic model Hamiltonian as

$$\widetilde{H}_0 = \widetilde{T}_z + V^{1D}_0(z_j), \tag{24}$$

where, based on our experiences detailed in [36,38], we use the following 11-point finite difference method [41] for the discretization of the kinetic energy operator T_z:

$$\widetilde{T}_z \Psi(z_j, t_k) = -\frac{1}{2\mu} \sum_{s=-5}^{5} c^{(5)}_{|s|} \Psi^{1D}(z_j + s\Delta z, t_k) \tag{25}$$

(see Table 1 of [41] for the coefficients c). This is accurate up to Δz^{10} for smooth functions (it is also limited by the Fourier representation). Then, the discrete Hamiltonian becomes an 11-banded diagonal matrix which operates on the column vector of the discretized wave function in coordinate

representation. Regarding the use of the atomic model potential in numerical simulations, this is the most important step since it defines the numerical eigensystem of the atom.

Regarding the time evolution, we use a three-step splitting of the $U(t, t+\Delta t)$ evolution operator which has an accuracy of Δt^4, and each of its substeps are propagated using the usual second-order Crank-Nicolson method [42] with a discrete second-order effective Hamiltonian (the particular formulas can be found in Secs. 3.1 and 4.1 in [36]). We find ground states and ground-state energies by performing imaginary time propagation [43,44]. For integrations, we use the quadrature formula $\int f(z)dz \approx \sum_j f(z_j)\Delta z$ because the numerical time evolution is unitary with respect to this summation.

When using the potential (22) the method described above can be applied without further complications. In the case of our density-based model potential a refinement is necessary as Eq. (21) is not differentiable in the origin, just as the true 3D Coulomb potential. Therefore, the ground state and energy of the discrete Hamiltonian (24) with $V_{0,\mathrm{M}}^{1\mathrm{D}}(z_j)$ is accurate only up to Δz^2. This is the reason why its ground-state density does not equal $\varrho_z^{100}(z_j)$ accurately enough, unless Δz is extremely small. We avoid this inaccuracy in the following way. Instead of $V_{0,\mathrm{M}}^{1\mathrm{D}}(z_j)$, we use its following discretized form in the computations:

$$\widetilde{V}_{0,\mathrm{M}}^{1\mathrm{D}}(z_j) = E_0 - \frac{1}{\psi_0(z_j)}\widetilde{T}_z\psi_0(z_j). \tag{26}$$

This definition of $\widetilde{V}_{0,\mathrm{M}}^{1\mathrm{D}}(z_j)$ ensures that the discretized ground-state vector $\psi_0(z_j)$ is the eigenvector of Eq. (24) with $\widetilde{V}_{0,\mathrm{M}}^{1\mathrm{D}}(z_j)$ and the corresponding energy is $\widetilde{E}_{0,\mathrm{M}} = E_0$, numerically exactly. The energy of the corresponding first excited state (with $\Delta z = 0.2$) is $\widetilde{E}_{1,\mathrm{M}} = -0.0904385$, which is close enough to $E_{1,\mathrm{M}}$. We have plotted the difference $\widetilde{V}_{0,\mathrm{M}}^{1\mathrm{D}}(z) - V_{0,\mathrm{M}}^{1\mathrm{D}}(z)$ in Fig. 1, magnified by a factor of 5.

The discretized form of the analytic model potential, $\widetilde{V}_{0,\mathrm{M}}^{1\mathrm{D}}(z_j)$, suggests also a modified discretization of the Dirac delta potential that we introduce as

$$\widetilde{V}_{0,\mathrm{DD}}^{1\mathrm{D}}(z_j) = E_{0,\mathrm{DD}} - \frac{1}{\psi_{0,\mathrm{DD}}(z_j)}\widetilde{T}_z\psi_{0,\mathrm{DD}}(z_j) \tag{27}$$

using the corresponding exact ground state $\psi_{0,\mathrm{DD}}(z_j)$ and energy $E_{0,\mathrm{DD}}$. This is a finite discretized potential which eliminates any singular feature from the corresponding Hamiltonian matrix. As we show in Appendix B, such definitions enable consistent and accurate simulations with high-order finite differences; therefore, it is a valid choice to define a potential using numerical inversion from its ground state.

V. RESULTS AND COMPARISON OF THE 1D AND 3D CALCULATIONS

In this section, we present and compare the results of strong-field simulations based on the 1D model potentials discussed in the previous sections. We selected the mean value of the dipole moment $\langle z\rangle(t)$ and its standard deviation $\sigma_z(t)$, the mean value of the velocity $\langle v_z\rangle(t)$, and the ground-state population loss $g(t)$ to characterize the dynamics resulting from the solutions of Eq. (8) with the various model potentials and from the solution of Eq. (6) as a reference. We also investigate the relation between the resulting various dipole power spectra $p(f)$, which is one of the most important quantities for high-order harmonic generation [17,45,46] and attosecond pulses. For the formulas of these physical quantities and for some details about the numerical accuracy of the simulations, see Appendixes A and B.

In these simulations, we model the linearly polarized few-cycle laser pulse with a sine-squared envelope function. The corresponding time-dependent electric field has nonzero values only in the interval $0 \leqslant t \leqslant N_{\mathrm{Cycle}}T$ according to the formula

$$\mathcal{E}_z(t) = F\sin^2\left(\frac{\pi t}{2N_{\mathrm{Cycle}}T}\right)\cos\left(\frac{2\pi t}{T}\right), \tag{28}$$

where T is the period of the carrier wave, F is the peak electric field strength, and N_{Cycle} is the number of cycles under the envelope function. Unless otherwise stated, we set $N_{\mathrm{Cycle}} = 3$ and $T = 100$; the latter corresponds to a ∼725 nm near-infrared carrier wavelength. From Fig. 2 on, the vertical dashed lines denote the zero crossings of the respective $\mathcal{E}_z(t)$ electric field.

We consider hydrogen in most of the simulations; i.e., we use $Z = 1$ and $\mu = 1$ if not otherwise stated explicitly. We set typically $\Delta z = 0.2$ and $\Delta t = 0.01$ since these are sufficient for the numerical errors to be within line thickness. We use box boundary conditions and we set the size of the box to be sufficiently large so that the reflections are kept below 10^{-8} atomic units.

The 3D reference results [i.e., the simulation results of the true 3D Schrödinger equation (6)] are plotted in Figs. 2–8 in blue and are labeled "3D-reference." The 1D simulation results and their respective colors are plotted as follows: our density-based model potential from numerical inversion (26) in purple, our improved soft-core Coulomb potential (22) in gold, our improved regularized Coulomb potential (23) in red, the conventional soft-core Coulomb potential (9) in green, and the discretized Dirac delta potential (11) in dark blue.

A. Low-frequency response

First, we discuss the results of a moderately strong laser pulse having a peak electric field value of $F = 0.1$. We plot the corresponding time-dependent mean values $\langle z\rangle(t)$ (the magnitude of which equals the dipole moment in atomic units) and their standard deviations $\sigma_z(t)$ in Fig. 2, and the time-dependent mean velocities $\langle v_z\rangle(t)$ and the ground-state population losses $g(t)$ in Fig. 3 for all the 1D model systems listed above. These curves justify that the simulation results obtained with our density-based model potential and the improved model potentials are already quantitatively comparable to the 3D results; i.e., these model potentials capture the essence of the 3D process. This fact is in strong contrast with the poor results of the conventional 1D soft-core and 1D Dirac delta potentials, which is caused mainly by their too-weak and too-strong binding forces, respectively.

The graphs of the improved soft-core Coulomb potential are clearly the closest to the 3D reference in most of these cases; i.e., this potential provides the quantitatively best model of the 3D case, despite that its ground-state density is not the exact reduced density of the 3D case. The results of our numerical density-based model potential are somewhat less close to the

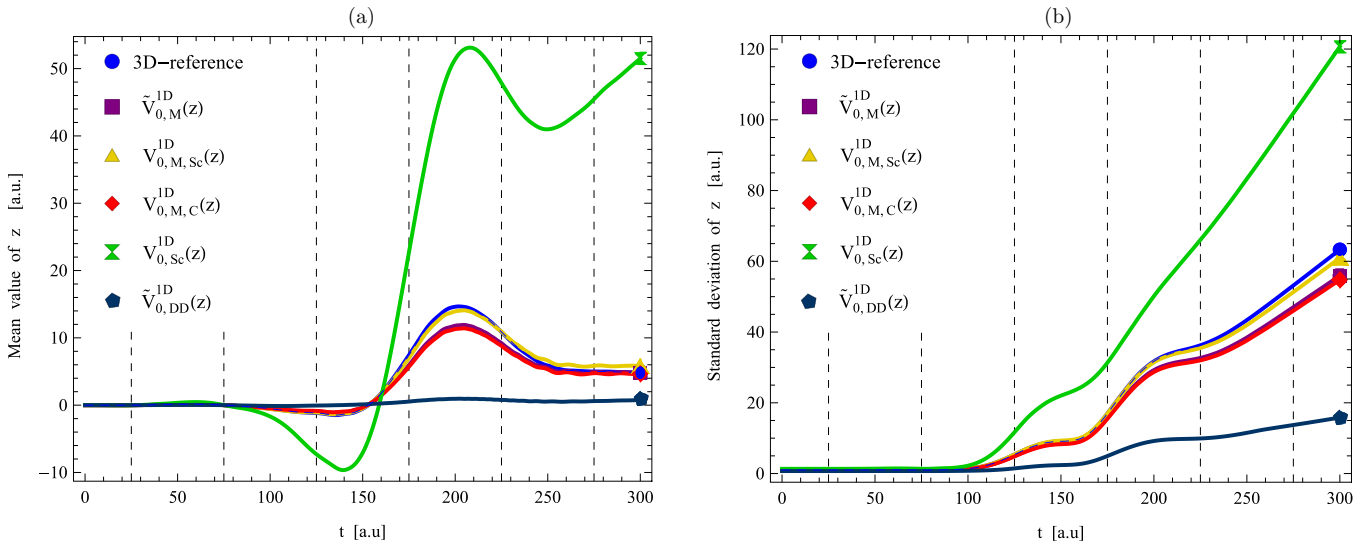

FIG. 2. Time dependence of (a) the mean values $\langle z\rangle(t)$ and (b) the standard deviations $\sigma_z(t)$ using different 1D model potentials, under the influence of the same external field with $F = 0.1$, $N_{\text{Cycle}} = 3$, and $T = 100$. Results of the corresponding 3D simulation are plotted in blue.

3D reference. Although these simulations start from the exact reduced density of the 3D case, the electron is somewhat more strongly bound to the ion core than is optimal. The results obtained using the improved regularized Coulomb potential are very close to those of the density-based model potential, but the former potential is even somewhat stronger than needed.

In a typical strong-field simulation, the ground-state population loss $g(t)$ is close to the probability of ionization. Due to the presence of the transverse degrees of freedom in three dimensions, it is then reasonable that the $g(t)$ values are somewhat larger in a 3D simulation than in one dimension. Note that the $g(t)$ curves of the 1D simulations follow very well the 3D reference curve in accordance with this.

The lack of the transverse degrees of freedom affects the $\langle v_z\rangle(t)$ curves of the 1D simulations in a different way: These exhibit the high-frequency oscillations with larger amplitude than the 3D reference curve. This can be explained by taking into account that rescattering on the ion core is a much stronger factor in one dimension, and that the integration over the transverse directions decreases the effect of the 3D density oscillations on the reduced mean values. We analyze this in more detail in the next section.

In order to demonstrate the capabilities of the density-based and the improved 1D model potentials, we selected the time-dependent dipole moment $\langle z\rangle(t)$ to present the results of four different scenarios in Figs. 4 and 5. Since the curves corresponding to the density-based model potential are very close to those corresponding to the improved regularized 1D Coulomb potential, we do not plot the $\langle z\rangle(t)$ of this latter potential in all of our figures.

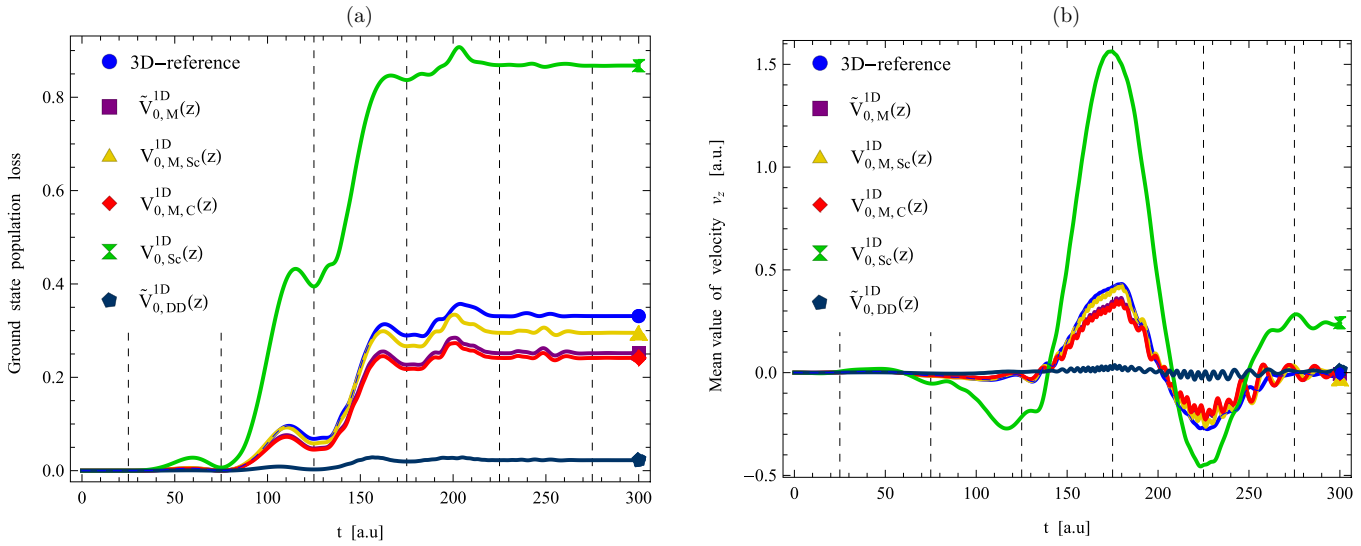

FIG. 3. Time dependence of (a) the ground-state population loss $g(t)$ and (b) the mean velocities $\langle v_z\rangle(t)$ using different 1D model potentials, under the influence of the same external field with $F = 0.1$, $N_{\text{Cycle}} = 3$, and $T = 100$. Results of the corresponding 3D simulation are plotted in blue.

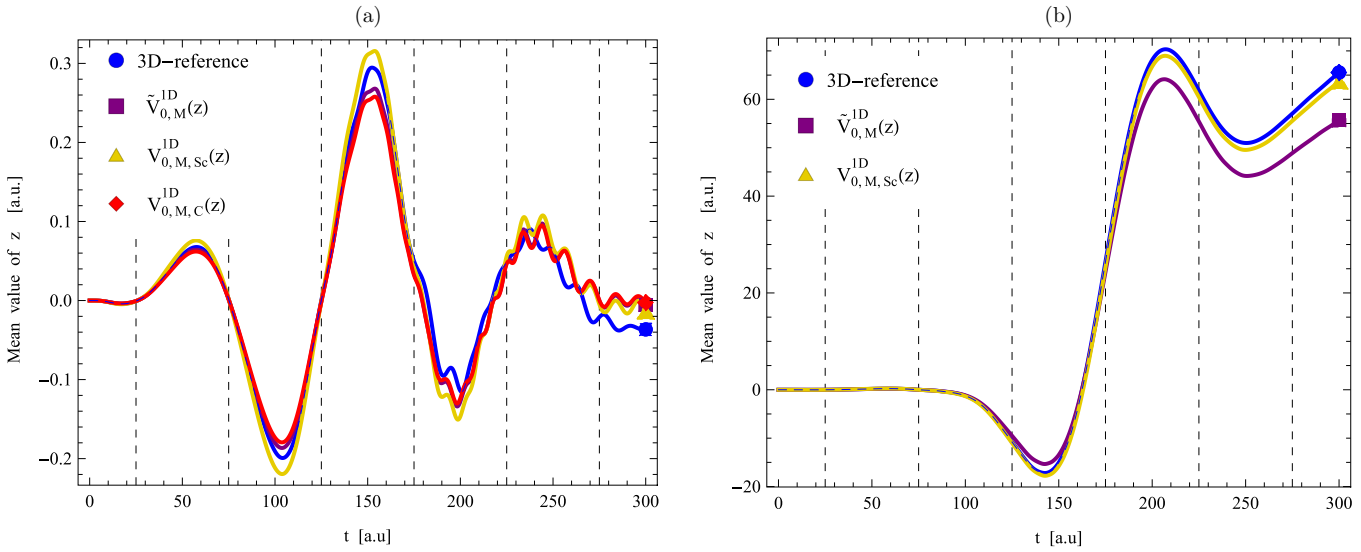

FIG. 4. Time dependence of mean values $\langle z \rangle(t)$ using different 1D model potentials, under the influence of the external field with (a) $F = 0.05$ and (b) $F = 0.15$, $N_{\text{Cycle}} = 3$, and $T = 100$. Results of the corresponding 3D simulations are plotted in blue.

In Fig. 4(a) we plot our simulation results for hydrogen, now with a weaker field of $F = 0.05$ which is in the tunnel ionization regime of hydrogen, while Fig. 4(b) corresponds to a stronger field of $F = 0.15$. Both of these figures clearly show that the improved 1D soft-core Coulomb potential provides the best results. Note that the change of F in the above range results in a change of more than two orders of magnitude in the peak value of $\langle z \rangle(t)$.

Figure 5(a) shows the results for a Ne atom driven by a field of $F = 0.15$. Here we model the 3D neon atom in the single active electron approximation [17] simply by setting the Coulomb charge $Z^{(\text{SAE})}_{\text{Ne}} = 1.25929$ in order to match the ionization potential to the experimental value. (For the improved regularized Coulomb potential $V^{1D}_{0,M,C}$ we set $a^{(\text{SAE})}_{\text{Ne}} \approx 0.26707525$, which yields $E_{0,M,C} \approx -0.792905$.)

The accuracy of these 1D results is somewhat lower around the peak and in the last half-period of the laser pulse than in the case of hydrogen, and the improved soft-core Coulomb potential performs considerably better overall than the two other model potentials. By changing the Coulomb charge Z within a reasonable range in order to model different noble gas atoms, we have obtained similarly accurate results.

Figure 5(b) shows $\langle z \rangle(t)$ for a hydrogen atom, now driven by a longer laser pulse of shorter carrier wavelength, corresponding to the parameters $T = 80$, $F = 0.1$, and $N_{\text{Cycle}} = 6$. The 1D model potentials work similarly accurately for this

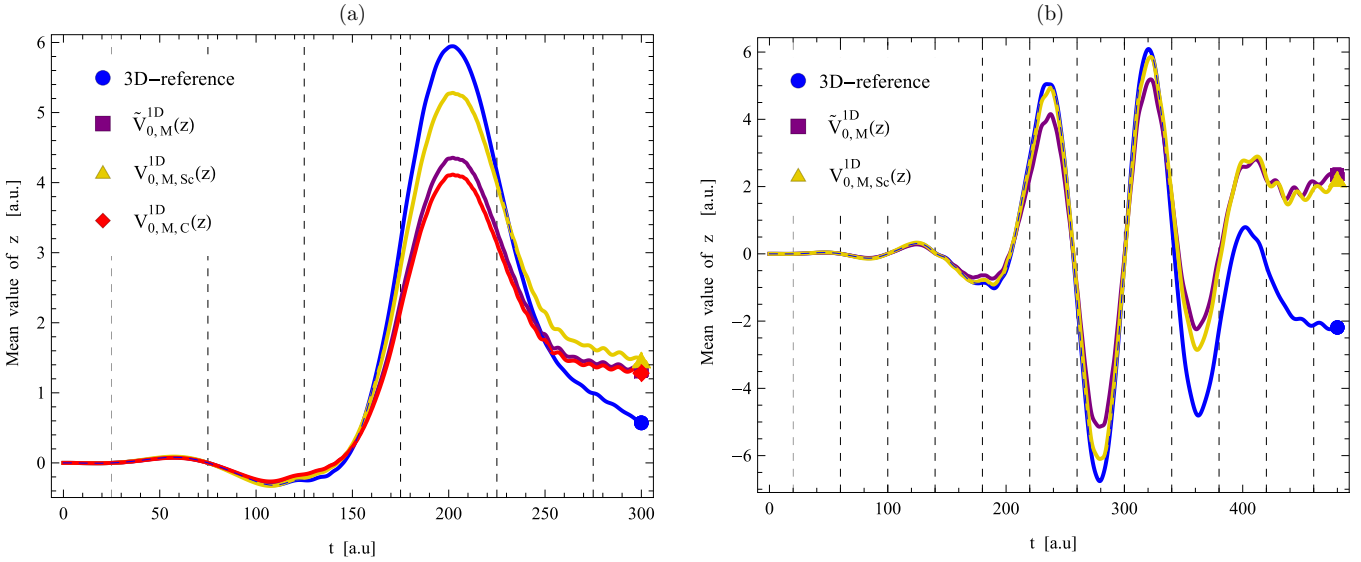

FIG. 5. Time dependence of mean values $\langle z \rangle(t)$ using different 1D model potentials. (a) Single active electron (SAE) model of a neon atom with $Z^{(\text{SAE})}_{\text{Ne}} = 1.25929$, driven by the external field with $T = 100$, $F = 0.15$, and $N_{\text{Cycle}} = 3$. (b) Hydrogen with $Z = 1$, driven by the external field with $T = 80$, $F = 0.1$, and $N_{\text{Cycle}} = 6$. Results of the corresponding 3D simulations are plotted in blue.

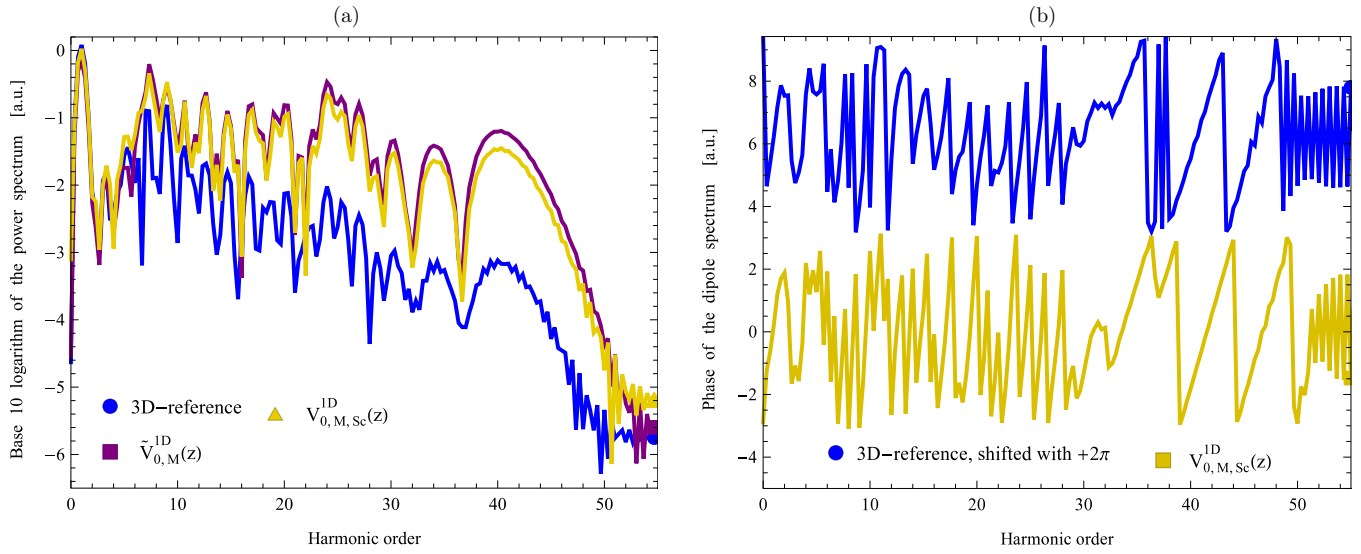

FIG. 6. (a) Logarithmic plot of the power spectra vs the harmonic order, i.e., $p(nf_1)$ (where $f_1 = 1/T = 0.01$ a.u. is the fundamental frequency). (b) Phase of the dipole acceleration spectra vs the harmonic order (upshifted by 2π for the 3D case). We plot the results for the density-based 1D model potential (purple) and for the improved soft-core Coulomb potential (gold) in comparison with the 3D reference (blue). The parameters $F = 0.1$, $N_{\text{Cycle}} = 3$, $T = 100$, and $Z = 1$ are the same as for Figs. 2 and 3.

longer laser pulse as in the case presented in Fig. 2(b), until the recollisions with the ion core gradually decrease the match between the 1D and 3D cases in the last two periods of the pulse.

Our density-based 1D model potential and both of the improved 1D model potentials exhibit an impressive improvement in the accuracy of the low-frequency response of typical strong-field processes, in contrast to the two conventional model potentials. These results are even more convincing if we take into account that $\langle z \rangle(t)$, $\sigma_z(t)$, and $g(t)$ are very sensitive to almost any change in the physical parameter values.

B. High-order harmonic spectra

In strong-field physics, the accurate computation of the high-order harmonic spectrum is especially important, because this represents the highly nonlinear atomic response to the strong-field excitation, with well-known characteristic features [6,45–48]. Besides the high-order harmonic yield, the suitable phase relations enable one to generate attosecond pulses of XUV light [1–3,49–52].

In Fig. 6(a), we plot the power spectrum of the dipole acceleration [see Eq. (A7)] for the parameters corresponding to Figs. 2 and 3.

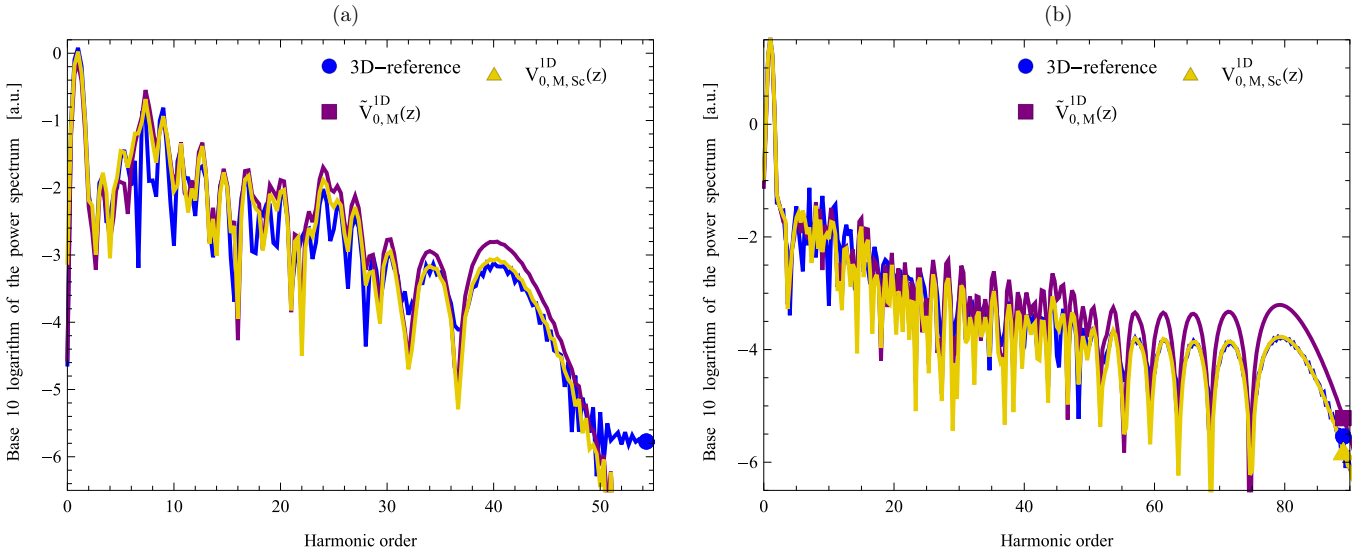

FIG. 7. Logarithmic plots of the scaled power spectra $p(nf_0)/s(nf_0)$ using the model systems of Fig. 6 with (a) $F = 0.10$ and (b) $F = 0.15$, in comparison with the 3D reference (blue).

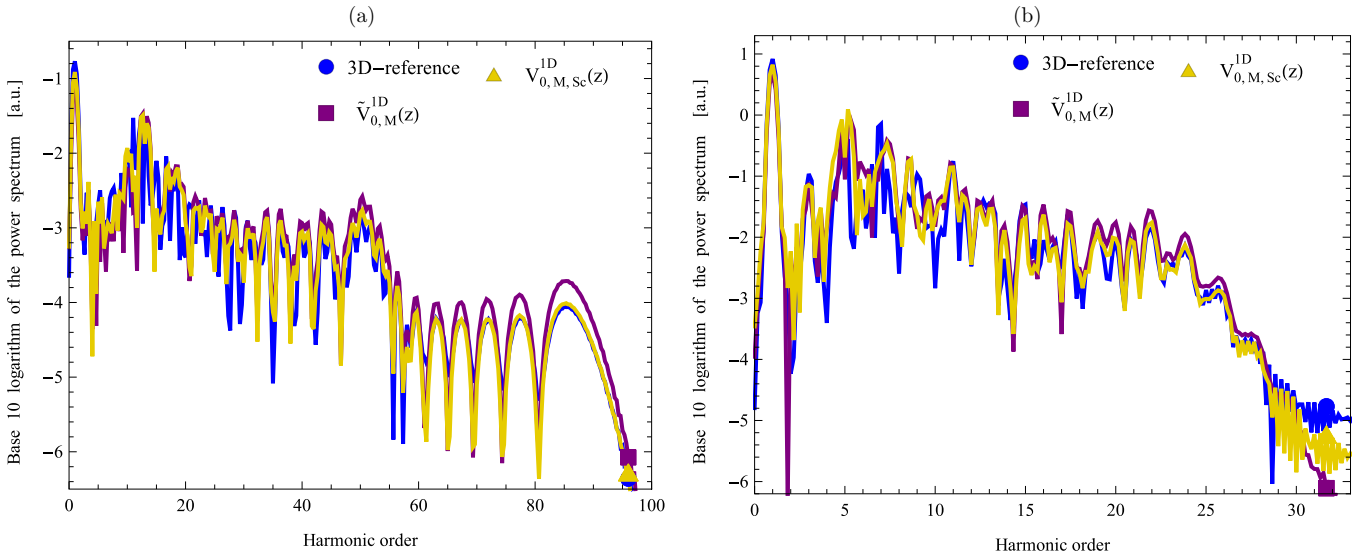

FIG. 8. Logarithmic plots of the scaled power spectra $p(nf_0)/s(nf_0)$ obtained using the density-based 1D model potential (purple) and the improved soft-core Coulomb potential (gold), in comparison with the 3D reference (blue). (a) Single active electron model of a neon atom with $Z^{(SAE)}_{Ne} = 1.25929$ driven by the external field with $T = 100$, $F = 0.15$, and $N_{Cycle} = 3$. (b) Hydrogen with $Z = 1$, driven by the external field with $T = 80$, $F = 0.1$, and $N_{Cycle} = 6$.

In agreement with the previous section, the power spectra obtained using the 1D model potentials agree very well with the 3D reference simulation result up to the fifth harmonic. For higher frequencies, the 1D spectra gradually deviate and give values that are one to two orders of magnitude larger than the 3D reference values. The explanation given for the oscillations of the $\langle v_z \rangle(t)$ curves in Fig. 3(b) applies also here: 1D simulations exaggerate the effect of the ion core, mainly via rescattering, while the effect of the 3D density oscillations weakens in the reduced mean values obtained from the 3D simulation.

However, the structure of the spectra in Fig. 6(a) is remarkably similar and the match of the spectral phase, shown in Fig. 6(b), is very good, especially in the higher frequency range, which is of fundamental importance for isolated attosecond pulses. These inspired us to create a scaling function which transforms the spectra obtained with the 1D simulation to fit the 3D reference spectrum as correctly as possible. Since the improved soft-core Coulomb potential (22) gives the best low-frequency results, we focus only on this model potential in the following.

Examination of the ratio of the magnitudes of the 1D power spectrum to the 3D power spectrum in our simulations with different parameters revealed that the scaling function

$$s(f) = \min(1 + 0.03(100f - 1)^2, 1 + |100f - 1|) \quad (29)$$

transforms the magnitude of the power spectra obtained using the improved 1D soft-core Coulomb potential to properly fit the corresponding 3D power spectra. In Fig. 7(a) we plot the scaled 1D power spectrum $p(f)/s(f)$ which gives a very good match between the 3D and 1D results in the case of the improved soft-core Coulomb potential. (Here and in the following figures we plot the scaled power spectrum of the density-based 1D model potential for completeness only.) In Figs. 7(b), 8(a), and 8(b) we present this comparison for three other scenarios, corresponding to the parameters of Figs. 4(b), 5(a), and 5(b), respectively. These plots clearly show that the scaling function (29) works very well also in these cases.

VI. DISCUSSION AND CONCLUSIONS

The results presented in the previous section demonstrate that it is possible to quantitatively model the true 3D quantum dynamics with the help of the density-based 1D model potential $\tilde{V}^{1D}_{0,M}(z_j)$ and the accordingly improved soft-core Coulomb potential $V^{1D}_{0,M,Sc}(z)$. The best results are obtained with the improved soft-core Coulomb potential (22), which is also very easy to use numerically. This means that we can perform quantum simulations of a single active electron atom driven by a strong linearly polarized laser pulse during a couple of minutes and obtain a fairly accurate low-frequency response and a reliable high-order harmonic generation (HHG) spectrum with the help of the scaling function (29). The simple form of this scaling is based on the good agreement between the structure and phase of the 1D and the 3D HHG spectra.

In achieving these results, the physical requirement about the 1D and 3D ground-state densities was the important starting idea. This led to the construction of the density-based 1D model potential, which then inspired the improved parametrization of the 1D soft-core Coulomb potential with effective charge $\frac{1}{2}Z$. Both of these have the same asymptotic tail which ensures that their ground-state energy is identical to that of the 3D system. The discretization of the density-based 1D model potential gave important lessons also about the numerical aspects of nondifferentiable 1D Coulomb-like potentials and the 1D delta potential.

Considering the obvious differences between the 1D and the 3D quantum dynamics and their effects, discussed already in connection with Figs. 3(b) and 6(a), it is not surprising that the high-frequency response of these 1D simulations is much stronger than that of the corresponding 3D case. The fact that the scaling function (29) has different frequency dependence

in the lower frequency domain than in the higher frequency domain, and that this seems to be independent of the other physical parameters, may hint at a deeper connection between the true 3D quantum dynamics and its best 1D model given by the improved soft-core Coulomb potential (22).

We expect that this improved soft-core Coulomb potential can be successfully used as a building block also in the 1D model of somewhat larger atomic systems, like a He atom, driven by a strong linearly polarized laser pulse. The method of construction of the reduced density-based 1D model potential could be used as well to create proper 1D model potentials for strong-field simulation of simple molecules, like $H_2{}^+$ or H_2.

ACKNOWLEDGMENTS

The authors thank F. Bogár, G. Paragi, and S. Varró for stimulating discussions. S.M. was supported by the UNKP-17-3 New National Excellence Program of the Ministry of Human Capacities of Hungary. The project has been supported by the European Union, co-financed by the European Social Fund, Grant No. EFOP-3.6.2-16-2017-00005. This work was supported by the GINOP-2.3.2-15-2016-00036 project. Partial support by the ELI-ALPS project is also acknowledged. The ELI-ALPS project (GOP-1.1.1-12/B-2012-000, GINOP-2.3.6-15-2015-00001) is supported by the European Union and co-financed by the European Regional Development Fund.

APPENDIX A: COMPARABLE PHYSICAL QUANTITIES IN ONE DIMENSION

For completeness, we list here the physical quantities that we use for characterizing the strong-field process, both in one and three dimensions.

From the 3D wave function we can calculate the 1D reduced density as

$$\varrho_z^{\mathrm{3D}}(z,t) = 2\pi \int_0^\infty |\Psi^{\mathrm{3D}}(z,\rho,t)|^2 \rho \, d\rho. \tag{A1}$$

In one dimension this is

$$\varrho_z^{\mathrm{1D}}(z,t) = |\Psi^{\mathrm{1D}}(z,t)|^2. \tag{A2}$$

We calculate the mean value of z as

$$\langle z\rangle(t) = \int_{-\infty}^{\infty} z\varrho_z(z,t)\, dz, \tag{A3}$$

the standard deviation of z as

$$\sigma_z(t) = \sqrt{\langle z^2\rangle(t) - \langle z\rangle^2(t)}, \tag{A4}$$

and the mean value of the z velocity and the z acceleration using the Ehrenfest theorems as

$$\langle v_z\rangle(t) = \frac{\partial\langle z\rangle}{\partial t}, \quad \langle a_z\rangle(t) = \frac{\partial\langle v_z\rangle}{\partial t}, \tag{A5}$$

in both the 3D and the 1D case. It is also interesting to determine the ground-state population loss

$$g(t) = 1 - |\langle\Psi(0)|\Psi(t)\rangle|^2, \tag{A6}$$

even though this refers to the population losses of two completely different states in one dimensions and three dimensions.

We calculate the spectrum from the dipole acceleration $\langle a_z\rangle$, and then the power spectrum as

$$p(f) = |\mathcal{F}[\langle a_z\rangle](f)|^2, \tag{A7}$$

where $\mathcal{F}$ denotes the Fourier transform and f is its frequency variable.

APPENDIX B: ACCURACY OF THE NUMERICAL INVERSION

1. Density-based 1D model potential

We stated previously that the numerical construction (26) yields the exact numerical eigensystem of that potential, but that does not give us the whole picture about how numerically accurate the construction really is. If we look at the eigenenergy of its respective first excited state calculated with $\Delta z = 0.2$ we see that it is accurate to four or five digits, but that alone does not determine the usefulness in strong-field simulations. To get the whole picture, we performed some numerical simulations using the atomic potential (26) and a three-cycle laser pulse of form (28) with $F = 0.1$ with different Δz parameters. We subtracted from them the results of a very accurate reference numerical solution using the analytic potential (21) with $\Delta z = 0.0001$, which gave us information about the (approximate) numerical errors of the construction.

The results can be seen in Fig. 9, where we plotted the errors of mean values $\langle z\rangle(t)$ and the ground-state population losses $g(t)$ compared to reference versus time. We can see that if we decrease the spatial step Δz of the inversion (26) from 0.4 (orange) to 0.2 (purple) the error decreases approximately by a factor of 16, in the cases of both $\langle z\rangle(t)$ and $g(t)$. We verified this using also other integrated quantities: we can clearly assert that the numerical inversion (26) is around Δz^4 accurate; i.e., it shows high-order accuracy (required that the kinetic energy operator is also at least Δz^4 accurate). To illustrate what this means, we also plotted the results obtained by the usual three-point finite difference Crank-Nicolson method (CN3) using the analytic potential (21) as the atomic potential, which is known to be Δz^2 accurate. We briefly note that we tested the direct use of Eq. (21) with our 11-point finite difference scheme but it was not any better—also Δz^2 accurate (since the potential is not differentiable)—so we only plotted the results of the CN3 scheme in Fig. 9 with green lines. The accuracy of this method using $\Delta z = 0.2$ is around 320 times better than the direct use of the analytic nondifferentiable potential with $\Delta z = 0.05$. So in other words it requires 2^6 more spatial grid points ($\Delta z \approx 0.003$) than the numerical inversion. Using formula (26) to numerically represent the (nonsingular) model potentials is very efficient and shows high-order convergence.

2. Delta potential

In the following, we discuss the accuracy tests of the numerically constructed potential (27) using strong-field simulations with the same three-cycle laser pulse of form (28) with $F = 0.1$ and different Δz parameters. For comparison we use a properly implemented method from [30] that uses the proper Robin boundary condition at $z = 0$, which overrides the Crank-Nicolson equations at that grid point. Its results

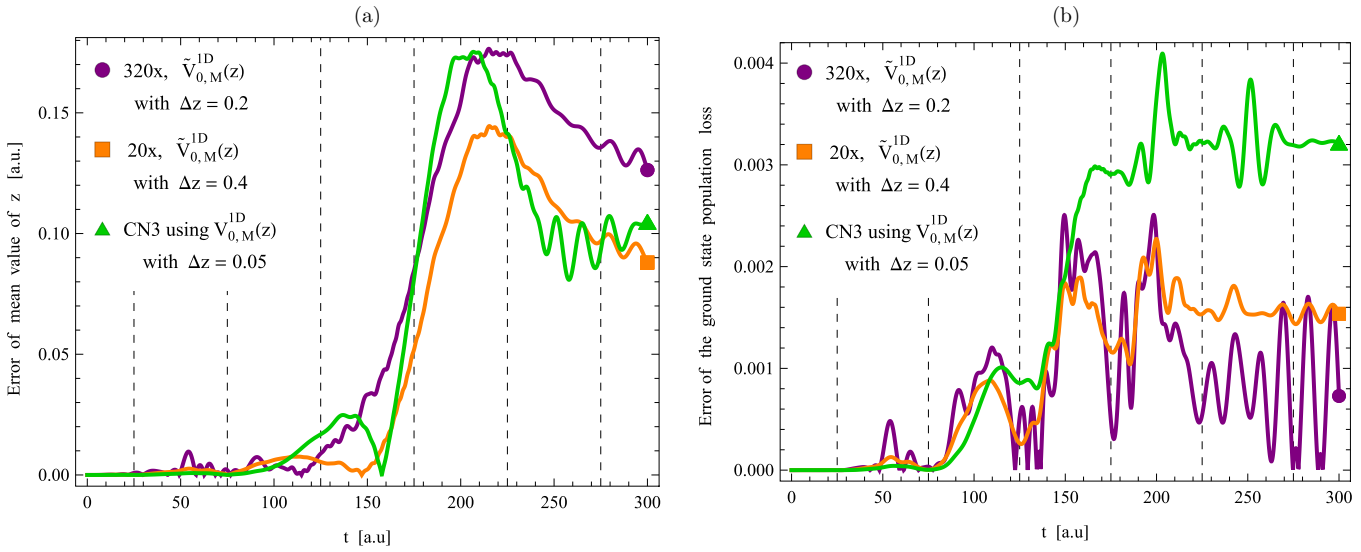

FIG. 9. Time dependence of (a) the numerical mean value errors $|\langle z\rangle(t) - \langle z\rangle_{\text{num,ref}}(t)|$ and (b) the ground-state population loss errors $|g(t) - g_{\text{num,ref}}(t)|$ using different realizations of the density-based model potentials, under the influence of the same external field with $F = 0.1$, $N_{\text{Cycle}} = 3$. We plotted in purple and orange the results using the potential $\tilde{V}^{1D}_{0,M}$ from numerical inversion formula (26) with $\Delta z = 0.2$ and $\Delta z = 0.4$, respectively. Note that the values of these two curves are magnified by factors of 320 and 20, as indicated. For comparison, we plotted in green the results directly using the analytic formula (21) as the atomic potential in an usual Crank-Nicolson solution.

are at least Δz^2 accurate. We calculate the errors of the mean values $\langle z\rangle(t)$ and the ground-state population losses $g(t)$ compared to a very accurate reference solution obtained by this correct method (uses $\Delta z = 0.001$). We can see the results in Fig. 10. Surprisingly, we can observe that the errors of Eq. (27) with $\Delta z = 0.2$ are actually not far from the errors of results obtained by the Δz^2 accurate proper method at $\Delta z = 0.05$. If we decrease the Δz step from 0.4 (orange) to 0.2 (dark blue) we see a factor-of-4 error decrease: We can conclude that the nonsingular construction (27) is actually correct numerical representation, and converges with Δz^2 even for the singular delta potential. It is also of importance because of the following: We can run simulations with singular potentials using nonsingular Hamiltonians, and the point of singularity does not have to be on the spatial grid; it can even move. It has even more interesting consequences in two or more dimensions, since there is no reason not to work with the true singular Coulomb potentials.

In conclusion, it is a valid choice to define a potential using numerical inversion from its ground state. It can provide a

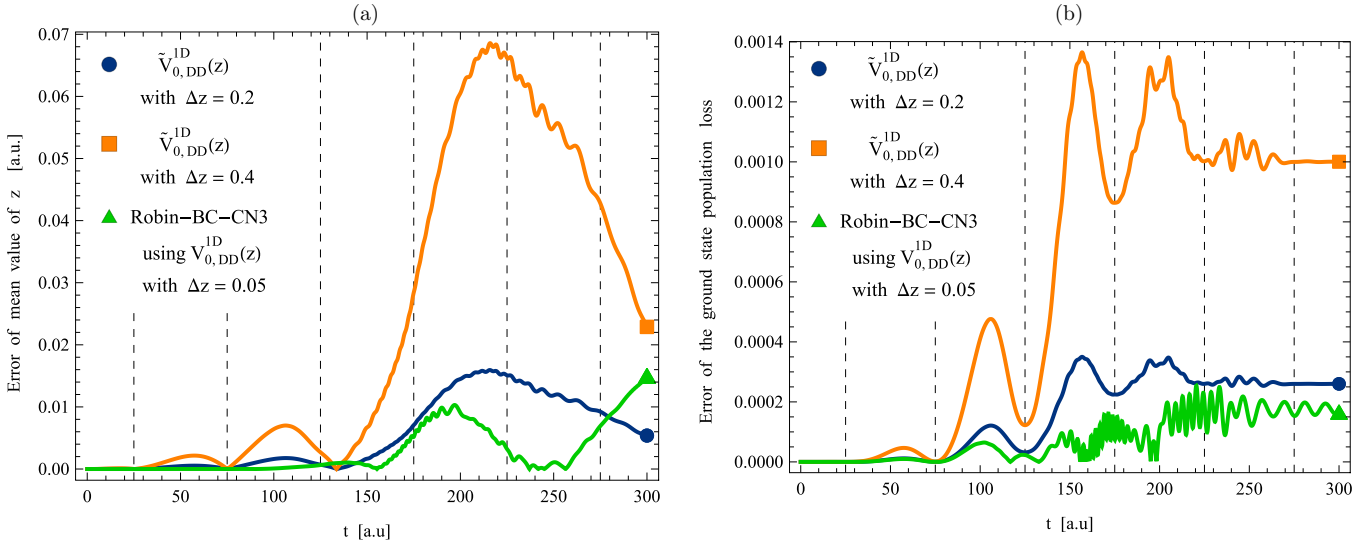

FIG. 10. Time dependence of (a) the numerical mean value errors $|\langle z\rangle(t) - \langle z\rangle_{\text{num,ref}}(t)|$ and (b) the ground-state population loss errors $|g(t) - g_{\text{num,ref}}(t)|$ using different implementations of the Dirac delta model potential, under the influence of the same external field with $F = 0.1$, $N_{\text{Cycle}} = 3$. We plotted in dark blue and orange the results using the potential $\tilde{V}^{1D}_{0,DD}$ from numerical inversion formula (27) with $\Delta z = 0.2$ and $\Delta z = 0.4$, respectively. For comparison, we plotted in green the results using the implementation in [30] that uses the proper Robin boundary condition to represent the singularity of Eq. (11).

consistent and accurate method with high-order finite differences to represent our Eq. (21) nonsingular and nondifferentiable atomic potential in one dimension, and even achieve Δz^4 convergence. The method is robust enough to provide Δz^2 convergence for the case of the singular 1D delta potential using Eq. (27).

[1] M. Hentschel, R. Kienberger, Ch. Spielmann, G. A. Reider, N. Milosevic, T. Brabec, P. Corkum, U. Heinzmann, M. Drescher, and F. Krausz, Attosecond metrology, Nature (London) **414**, 509 (2001).

[2] R. Kienberger, M. Hentschel, M. Uiberacker, Ch. Spielmann, M. Kitzler, A. Scrinzi, M. Wieland, Th. Westerwalbesloh, U. Kleineberg, U. Heinzmann *et al.*, Steering attosecond electron wave packets with light, Science **297**, 1144 (2002).

[3] M. Drescher, M. Hentschel, R. Kienberger, M. Uiberacker, V. Yakovlev, A. Scrinzi, Th. Westerwalbesloh, U. Kleineberg, U. Heinzmann, and F. Krausz, Time-resolved atomic inner-shell spectroscopy, Nature (London) **419**, 803 (2002).

[4] A. Baltuška, Th. Udem, M. Uiberacker, M. Hentschel, E. Goulielmakis, Ch. Gohle, R. Holzwarth, V. S. Yakovlev, A. Scrinzi, T. W. Hänsch *et al.*, Attosecond control of electronic processes by intense light fields, Nature (London) **421**, 611 (2003).

[5] M. Uiberacker, Th. Uphues, M. Schultze, A. J. Verhoef, V. Yakovlev, M. F. Kling, J. Rauschenberger, N. M. Kabachnik, H. Schröder, M. Lezius *et al.*, Attosecond real-time observation of electron tunnelling in atoms, Nature (London) **446**, 627 (2007).

[6] F. Krausz and M. Ivanov, Attosecond physics, Rev. Mod. Phys. **81**, 163 (2009).

[7] P. Hommelhoff, C. Kealhofer, A. Aghajani-Talesh, Y. R. P. Sortais, S. M. Foreman, and M. A. Kasevich, Extreme localization of electrons in space and time, Ultramicroscopy **109**, 423 (2009).

[8] M. Schultze, M. Fieß, N. Karpowicz, J. Gagnon, M. Korbman, M. Hofstetter, S. Neppl, A. L. Cavalieri, Y. Komninos, Th. Mercouris *et al.*, Delay in photoemission, Science **328**, 1658 (2010).

[9] S. Haessler, J. Caillat, W. Boutu, C. Giovanetti-Teixeira, T. Ruchon, T. Auguste, Z. Diveki, P. Breger, A. Maquet, B. Carré *et al.*, Attosecond imaging of molecular electronic wavepackets, Nat. Phys. **6**, 200 (2010).

[10] A. N. Pfeiffer, C. Cirelli, M. Smolarski, D. Dimitrovski, M. Abu-Samha, L. B. Madsen, and U. Keller, Attoclock reveals natural coordinates of the laser-induced tunnelling current flow in atoms, Nat. Phys. **8**, 76 (2012).

[11] D. Shafir, H. Soifer, B. D. Bruner, M. Dagan, Y. Mairesse, S. Patchkovskii, M. Yu. Ivanov, O. Smirnova, and N. Dudovich, Resolving the time when an electron exits a tunnelling barrier, Nature (London) **485**, 343 (2012).

[12] P. Ranitovic, C. W. Hogle, P. Rivière, A. Palacios, X.-M. Tong, N. Toshima, A. González-Castrillo, L. Martin, F. Martín, M. M. Murnane *et al.*, Attosecond vacuum UV coherent control of molecular dynamics, Proc. Natl. Acad. Sci. USA **111**, 912 (2014).

[13] L.-Y. Peng, W.-C. Jiang, J.-W. Geng, W.-H. Xiong, and Q. Gong, Tracing and controlling electronic dynamics in atoms and molecules by attosecond pulses, Phys. Rep. **575**, 1 (2015).

[14] M. F. Ciappina, J. A. Pérez-Hernández, A. S. Landsman, W. A. Okell, S. Zherebtsov, B. Förg, J. Schötz, L. Seiffert, T. Fennel, T. Shaaran *et al.*, Attosecond physics at the nanoscale, Rep. Prog. Phys. **80**, 054401 (2017).

[15] L. V. Keldysh, Ionization in the field of a strong electromagnetic wave, Sov. Phys. JETP **20**, 1307 (1965).

[16] S. Varró and F. Ehlotzky, A new integral equation for treating high-intensity multiphoton processes, Nuovo Cimento D **15**, 1371 (1993).

[17] M. Lewenstein, P. Balcou, M. Yu. Ivanov, A. L'Huillier, and P. B. Corkum, Theory of high-harmonic generation by low-frequency laser fields, Phys. Rev. A **49**, 2117 (1994).

[18] M. Protopapas, D. G. Lappas, and P. L. Knight, Strong Field Ionization in Arbitrary Laser Polarizations, Phys. Rev. Lett. **79**, 4550 (1997).

[19] M. Yu. Ivanov, M. Spanner, and O. Smirnova, Anatomy of strong field ionization, J. Mod. Opt. **52**, 165 (2005).

[20] A. Gordon, R. Santra, and F. X. Kärtner, Role of the Coulomb singularity in high-order harmonic generation, Phys. Rev. A **72**, 063411 (2005).

[21] M. V. Frolov, N. L. Manakov, A. M. Popov, O. V. Tikhonova, E. A. Volkova, A. A. Silaev, N. V. Vvedenskii, and A. F. Starace, Analytic theory of high-order-harmonic generation by an intense few-cycle laser pulse, Phys. Rev. A **85**, 033416 (2012).

[22] J. Javanainen, J. H. Eberly, and Q. Su, Numerical simulations of multiphoton ionization and above-threshold electron spectra, Phys. Rev. A **38**, 3430 (1988).

[23] Q. Su and J. H. Eberly, Model atom for multiphoton physics, Phys. Rev. A **44**, 5997 (1991).

[24] D. Bauer, Two-dimensional, two-electron model atom in a laser pulse: Exact treatment, single-active-electron analysis, time-dependent density-functional theory, classical calculations, and nonsequential ionization, Phys. Rev. A **56**, 3028 (1997).

[25] C. C. Chirilă, I. Dreissigacker, E. V. van der Zwan, and M. Lein, Emission times in high-order harmonic generation, Phys. Rev. A **81**, 033412 (2010).

[26] A. A. Silaev, M. Yu. Ryabikin, and N. V. Vvedenskii, Strong-field phenomena caused by ultrashort laser pulses: Effective one- and two-dimensional quantum-mechanical descriptions, Phys. Rev. A **82**, 033416 (2010).

[27] K. A. Sveshnikov and D. I. Khomovskii, Schrödinger and Dirac particles in quasi-one-dimensional systems with a Coulomb interaction, Theor. Math. Phys. **173**, 1587 (2012).

[28] S. Gräfe, J. Doose, and J. Burgdörfer, Quantum phase-space analysis of electronic rescattering dynamics in intense few-cycle laser fields, J. Phys. B **45**, 055002 (2012).

[29] A. Czirják, R. Kopold, W. Becker, M. Kleber, and W. P. Schleich, The Wigner function for tunneling in a uniform static electric field, Opt. Commun. **179**, 29 (2000).

[30] A. Czirják, S. Majorosi, J. Kovács, and M. G. Benedict, Emergence of oscillations in quantum entanglement during rescattering, Phys. Scr. **T153**, 014013 (2013).

[31] S. Geltman, Bound states in delta function potentials, J. At. Mol. Opt. Phys. **2011**, 573179 (2011).

[32] C. Baumann, H.-J. Kull, and G. M. Fraiman, Wigner representation of ionization and scattering in strong laser fields, Phys. Rev. A **92**, 063420 (2015).

[33] N. Teeny, E. Yakaboylu, H. Bauke, and C. H. Keitel, Ionization Time and Exit Momentum in Strong-Field Tunnel Ionization, Phys. Rev. Lett. **116**, 063003 (2016).

[34] D. J. Griffiths, *Introduction to Quantum Mechanics* (Pearson Prentice Hall, Upper Saddle River, NJ, 2005).

[35] B. H. Bransden and C. J. Joachain, *Physics of Atoms and Molecules* (Prentice Hall, New York, 2003).

[36] S. Majorosi and A. Czirják, Fourth order real space solver for the time-dependent Schrödinger equation with singular Coulomb potential, Comput. Phys. Commun. **208**, 9 (2016).

[37] A. D. Bandrauk, S. Chelkowski, D. J. Diestler, J. Manz, and K.-J. Yuan, Quantum simulation of high-order harmonic spectra of the hydrogen atom, Phys. Rev. A **79**, 023403 (2009).

[38] S. Majorosi, M. G. Benedict, and A. Czirják, Quantum entanglement in strong-field ionization, Phys. Rev. A **96**, 043412 (2017).

[39] C. A. Ullrich, *Time-Dependent Density-Functional Theory: Concepts and Applications* (Oxford University Press, Oxford, UK, 2011).

[40] W. Kohn and L. J. Sham, Self-consistent equations including exchange and correlation effects, Phys. Rev. **140**, A1133 (1965).

[41] W. van Dijk and F. M. Toyama, Accurate numerical solutions of the time-dependent Schrödinger equation, Phys. Rev. E **75**, 036707 (2007).

[42] W. H. Press, S. A. Teukolsky, W. T. Vetterling, and B. P. Flannery, *Numerical Recipes 3rd Edition: The Art of Scientific Computing* (Cambridge University Press, Cambridge, UK, 2007).

[43] D. Bauer and P. Koval, QPROP: A Schrödinger-solver for intense laser–atom interaction, Comput. Phys. Commun. **174**, 396 (2006).

[44] S. A. Chin, S. Janecek, and E. Krotscheck, Any order imaginary time propagation method for solving the Schrödinger equation, Chem. Phys. Lett. **470**, 342 (2009).

[45] A. McPherson, G. Gibson, H. Jara, U. Johann, T. S. Luk, I. A. McIntyre, K. Boyer, and C. K. Rhodes, Studies of multiphoton production of vacuum-ultraviolet radiation in the rare gases, J. Opt. Soc. Am. B **4**, 595 (1987).

[46] S. E. Harris, J. J. Macklin, and T. W. Hänsch, Atomic scale temporal structure inherent to high-order harmonic generation, Opt. Commun. **100**, 487 (1993).

[47] M. Ferray, A. L'Huillier, X. F. Li, L. A. Lompre, G. Mainfray, and C. Manus, Multiple-harmonic conversion of 1064 nm radiation in rare gases, J. Phys. B: At. Mol. Opt. Phys. **21**, L31 (1988).

[48] Á. Gombkötő, A. Czirják, S. Varró, and P. Földi, Quantum-optical model for the dynamics of high-order-harmonic generation, Phys. Rev. A **94**, 013853 (2016).

[49] Gy. Farkas and Cs. Tóth, Proposal for attosecond light pulse generation using laser induced multiple-harmonic conversion processes in rare gases, Phys. Lett. A **168**, 447 (1992).

[50] P. M. Paul, E. S. Toma, P. Breger, G. Mullot, F. Augé, Ph. Balcou, H. G. Muller, and P. Agostini, Observation of a train of attosecond pulses from high harmonic generation, Science **292**, 1689 (2001).

[51] J. J. Carrera, X.-M. Tong, and S.-I. Chu, Creation and control of a single coherent attosecond XUV pulse by few-cycle intense laser pulses, Phys. Rev. A **74**, 023404 (2006).

[52] G. Sansone, E. Benedetti, F. Calegari, C. Vozzi, L. Avaldi, R. Flammini, L. Poletto, P. Villoresi, C. Altucci, R. Velotta *et al.*, Isolated single-cycle attosecond pulses, Science **314**, 443 (2006).